Published in final edited form as:

Magn Reson Med. 2006 December ; 56(6): 1274–1282. doi:10.1002/mrm.21073.

9.4T Human MRI: Preliminary Results

Thomas Vaughan[1,2,3,*], **Lance DelaBarre**[1], **Carl Snyder**[1], **Jinfeng Tian**[1,3], **Can Akgun**[1], **Devashish Shrivastava**[1], **Wanzahn Liu**[1], **Chris Olson**[2], **Gregor Adriany**[1], **John Strupp**[1], **Peter Andersen**[1], **Anand Gopinath**[2], **Pierre-Francois van de Moortele**[1], **Michael Garwood**[1], and **Kamil Ugurbil**[1,3]

[1]Department of Radiology, Center for Magnetic Resonance Research, University of Minnesota, Minneapolis, Minnesota, USA

[2]Department of Electrical Engineering, University of Minnesota, Minneapolis, Minnesota, USA

[3]Department of Biomedical Engineering, University of Minnesota, Minneapolis, Minnesota, USA

Abstract

This work reports the preliminary results of the first human images at the new high-field benchmark of 9.4T. A 65-cm-diameter bore magnet was used together with an asymmetric 40-cm-diameter head gradient and shim set. A multichannel transmission line (transverse electromagnetic (TEM)) head coil was driven by a programmable parallel transceiver to control the relative phase and magnitude of each channel independently. These new RF field control methods facilitated compensation for RF artifacts attributed to destructive interference patterns, in order to achieve homogeneous 9.4T head images or localize anatomic targets. Prior to FDA investigational device exemptions (IDEs) and internal review board (IRB)-approved human studies, preliminary RF safety studies were performed on porcine models. These data are reported together with exit interview results from the first 44 human volunteers. Although several points for improvement are discussed, the preliminary results demonstrate the feasibility of safe and successful human imaging at 9.4T.

Keywords

9.4T human MRI; B_1 shimming; multi-channel transmit; high field MRI

The impetus for this work originated with the first 9.4T primate images obtained from a large male cynomolgus macaque at the University of Minnesota's Center for Magnetic Resonance Research in 1995 (1). In that early study, the signal-to-noise ratio (SNR) at 9.4T more than doubled the SNR reported at the time for 4T human results (2–5). The RF uniformity and specific absorption rate (SAR) for the monkey study were high and low, respectively. These data also validated the technology and methodology developed to achieve successful 9.4T results in larger laboratory animals. Based on these preliminary results and the need to double the SNR and spectral resolution in laboratory primate studies

[*]Correspondence to: Thomas Vaughan, CMRR, University of Minnesota, 2021 Sixth St. SE, Minneapolis, MN 55455. tommy@cmrr.umn.edu.

from the commonly used 4.7T field strength, an initial "seed" grant was awarded in 1997 for what would eventually become the 9.4T system of this report (6). Significant support from the Keck Foundation, the University of Minnesota, and other sources made the present 9.4T system and facility possible.

As reported, the macaque head examined in Ref. 1 had only one-seventh the volume of an adult human head. While the SNR and spectral resolution from that study should predict human results, the uniform RF field contours in the monkey head at 9.4T would not predict the B_1 field in the human head of significantly greater electrical dimension. Prior to the present study, predictions of human images at 400 MHz Larmor frequencies were extrapolated upward from 7T data (7), downward from 11.1T images of fixed brains ex vivo (8), or directly from head-coil bench studies (9) and numerical models at 400 MHz, as presented in this article. Data from all four sources predicted severe RF artifacts for images achieved by the conventional means of placing a human head inside a homogeneous, circularly polarized volume coil that is resonant at 400 MHz. These high-frequency RF artifacts were first reported as a "dielectric resonance" (2). Since those first observations were made, high-field-dependent head imaging artifacts have been widely reported and explained (5,10–15). Our current understanding is that regions of signal deficit in a brain image are due to regions of destructive interference enhanced and exacerbated by the increasingly shortened wavelength of the incident RF (B_1) field in the brain dielectric (16,17). Several means of correcting these RF artifacts have been proposed, including adiabatic RF pulses (18), dielectric lensing (19), and B_1 shimming (5,13,16,20–23). The latter method was employed to good effect in the present study.

MATERIALS AND METHODS

The attempt to reach a 9.4T field strength for human imaging applications required new technology and methodology. The magnet used in this study was installed in April 2004 in a new facility at the Center for Magnetic Resonance Research, University of Minnesota (Minneapolis, MN, USA). Surrounding the magnet is a rectangular box shield comprised of 350 tons of welded plate steel that is 8" thick at the magnet center and tapers to 1" thick at the end plates. The end plates contain a window and a door on the system user end, balancing a brass plate bulk head (patch panel) access on the opposite end. Also enclosing the magnet and incorporating the steel magnet shield is an RF enclosure (Lindgren RF Enclosures, Inc., Glendale Heights, IL, USA) to isolate the magnet environment from outside signals by 110 dB at 400 MHz. Within the magnet is an asymmetric head gradient and shim set, also of Magnex design and manufacture. Subject access to the magnet is provided by a computer-controlled motorized cantilevered table to regulate entry speed (High Field NMR Systems, Inc., Birmingham, AL, USA). Velocities of 1–2 cm/s (continuously variable from zero) were used in this study. Interfacing the magnet is a custom RF system featuring a new multichannel, parallel transceiver (24) (see Figs. 1b and 2). The RF coils and digital receivers were built in-house (Fig. 1c and d). The programmable transmit phase and magnitude (gain) controllers were designed in-house and manufactured by Communications Power Corp. (Hauppauge, NY, USA), which also produced the 16, 500-W RF power amplifiers for the system. An Inova spectrometer console (Varian, Inc., Palo

Alto, CA, USA) controlled the system data-acquisition functions. The specifications of the magnet, gradients, shims, and RF systems are described below.

Magnet Subsystem

The magnet (Magnex model MRBR 9.4T/650) shown in Fig. 1a is a complete superconducting magnet system that is intended primarily for laboratory primate and human research. The system consists of a highly homogeneous superconducting magnet housed in a horizontal room-temperature bore, low-loss helium cryostat. Magnet field shimming is mainly accomplished with the use of superconducting shim coils. Final shimming is performed with a small amount of passive shim material and very fine use of the room-temperature shims. The system is also configured with twin cryo-refrigerators to minimize helium consumption and to eliminate the necessity for a liquid nitrogen reservoir. The multicoil superconducting magnet is constructed with a 354-km multifilament NbTi conductor carrying 218 amps with 78 MJ of stored energy. Field drift is less than 0.05 ppm/hr. Field homogeneity over a 30-cm sphere with superconducting shims is ±2.5 ppm, and with passive shims added it is ±1.5 ppm. The 5-gauss fringe field of this magnet extends to 20.2 m axially and 16 m radially from the magnet center. This is reduced by the passive steel shielding built into the room walls measuring 11.9 m by 4.7 m. The magnet coils are protected from quench damage by a resistor and diode network in the helium reservoir. The superconducting shim coils are positioned on a nonconducting former surrounding the main coil in the helium reservoir. Each coil set is fitted with a superconducting switch for persistent mode operation. The shim coils included are Z1, Z2, Z3, X, Y, ZX, ZY, X2-Y2, XY, Z2X, Z2Y, Z(X2-Y2), and ZXY. Each coil is rated to carry a maximum current of 25 amps. All shims are designed to be decoupled from the main coil.

Cryostat

The cryostat is of conventional design and consists of a central all-welded stainless steel helium vessel that is surrounded by two aluminum gas-cooled radiation shields. The cryostat measures 3.15 m long and 3.48 m high, with a 0.65-m clear bore. It weighs 30 tons without cryogens. The complete assembly is contained in a stainless-steel outer vacuum vessel with a vertical service turret located centrally on top of the cryostat. The turret provides access to the helium reservoir for the demountable magnet leads, helium level probe, and helium transfer siphon. The system is equipped with two Leybold model 5100 two-stage cryocoolers with CP6000 compressor units. The helium reservoir contains 2500 L of liquid helium with 1600 L volume above the refill level. The liquid helium evaporation rate is 0.2 L/ hr, and the refill interval is 6 months.

Gradients and Shims

The magnet is fitted with an asymmetric, torque-compensated, self-shielded “head” gradient and shim set (Magnex model SGRAD III 640/400/SP). The dimensions include a 160-cm length, 64-cm outer diameter (o.d.), and 40-cm inner diameter (i.d.) with the isocenter displaced 18 cm from the utility end to give ample access for human head and laboratory primate imaging and spectroscopy. The peak operating voltage is 1 kV, and the peak current is 500 amps with 180A RMS. At 80% peak current, the gradient strength is 40 mT/m and the fastest 0–98% rise-time for the X, Y, and Z gradients is 150 μs. For routine imaging, the

amplitude is limited to 40 mT/m, and the rise-time is set to 250 μs. The gradient is powered by a Siemens Sonata Gradient Engine set to these specifications. The shim set includes an actively shielded Z_0 shim for B_0 correction, a set of high-power, second-order resistive shims (Z0, Z2, ZX, ZY, 2XY, X2-Y2), and a 24-tray passive shim system in the cryostat.

Console

A Varian Unity Inova console was interfaced to the 9.4T magnet system and used to generate the data in this report. The console configuration employed a Sun Blade 2500 (Sun Microsystems, Inc., Santa Clara, CA, USA) as a host workstation to control the transmit excite signal and data acquisition through single proton frequency transmit and receive channels, respectively. This console was modified in-house to transmit and receive initially on eight channels and then on 16 channels each. Each of the multiple receiver channels was mixed to an intermediate frequency (IF) signal of 20 MHz and then oversampled at 64 MHz by 14 bit ADCs on Echotek ECDR-814 digital receiver boards (Echotek, Inc., Huntsville, AL, USA) for an effective 20 bits after filtering and decimation to a spectral width of 10 kHz. The digital receiver boards were housed in a VME64x card cage chassis with a Motorola MVME5500 single-board computer (Motorola Embedded Communications Computing, Tempe, AZ, USA) as the bus master that runs custom-written control software under the VxWorks operating systems (Wind River, Alameda, CA, USA). A second Sun Blade 2500 workstation was added to increase the data-handling capacity needed to process and store the data from the multiple receive channels. Active diode-protected, decoupling preamplifiers were custom designed for the multichannel transverse electromagnetic (TEM) coil interface. The console's single proton frequency transmit channel was split into multiple, parallel paths at the 1-mW level. Programmable phase shifters (360° range, 1.4° resolution) and attenuators (64-dB range, 0.25-dB resolution) were included in each transmit path to provide for console-controlled phase and magnitude for each channel. Each channel was then amplified by 500-W broadband amplifiers (30 – 405 MHz) and independently switched in time by channel-dedicated transmit-receive switches. Additional details of the RF parallel transceiver system and applications are provided below.

RF Methods

Modeling—RF-related artifacts have been well documented for human imaging at 7T (7,17,25,26). To explore the nature and extent of this problem at 9.4T, we constructed XFDTD models (Remcom Inc., College Station, PA, USA) of a human head inside a conventional inductively driven, circularly polarized TEM head resonator. The coil was of clinical standard 27.5 cm i.d. and generated a uniform B_1 field in free space. When the NLM Visual Human male head was added to the model, the B_1 field uniformity across the head was severely degraded, as shown in the three center planes of the 3D model in Fig. 3. The patterns of nonuniformity are similar to those seen in 7T images, but are more severe (7). These exploratory models and other data indicate that conventional volume coils of circularly polarized, uniform fields used at lower frequencies will be suboptimal for use at 9.4T. Therefore, new coil designs and application methods are required.

B_1 Shimming

Adjusting the relative magnitude and phase of independent current elements in a coil structure has been shown to compensate for high-field RF artifacts by means that were first described by our group as "B_1 shimming" (5,13,16,19,27,28). Controlling the phase angle and magnitude of the RF signal on separate coil elements can be accomplished by manual means, such as trimming the coaxial cable lengths and adding coaxial attenuators (25). However, these mechanical approaches to coil field control are laborious and time-intensive, and do not lend themselves to feedback-driven algorithms for interactive and automatic image optimization. To resolve these problems, an electronic computer-controlled "parallel transceiver" was developed for the RF front end of the 9.4T system (24,26,29).

The parallel transceiver (see Fig. 1a and b for a photograph, and Fig. 2 for a diagram) combines a multichannel parallel transmitter and a multichannel digital receiver into one integrated system. In Fig. 2, a low-level, shaped transmit signal from the console is split into multiple equal phase and magnitude signals. Each of the split signal paths is independently modulated via console control by programmable phase shifters and attenuators. The modulated signals are then amplified by multiple channel-dedicated RF power amplifiers. The transmit-receive switches temporally isolate the transmit from the receive signals at each coil element. The signal from each coil element is acquired by a dedicated preamplifier, which feeds the multichannel digital receiver. In static operational mode, the phase and magnitude can be set to a fixed value. In the dynamic mode, phase and magnitude information is currently accessed from values stored in a lookup table and is changed on reception of an update trigger signal. Communication with the phase and gain controller is achieved through 100 Base-T Ethernet.

B_1 Localization

As modeled in Fig. 3, 9-cm wavelengths in the human brain imaged at 9.4T lead to pronounced B_1 field contours and hence image inhomogeneity. If these B_1 field gradients can be controlled over a volume, it may be possible to steer a constructively interfering field node to spatially correlate with an anatomic region of interest (ROI). One such technique for ROI localization was modeled in this study, as described below.

The 16-element, multichannel TEM head coil (Fig. 1d) was modeled together with a cylindrical phantom of physiologic electrical parameters for 400 MHz. The coil measured 28 cm i.d. × 34.5 cm o.d. × 18 cm long, and the phantom centered within the coil was 20 cm diameter by 20 cm long. Maxwell solutions for the 3D model were numerically calculated by the finite element method (FEM). Simulations in which each coil element was driven independently were first performed to determine the phantom response to individual drives. The B_1 field at a point in the phantom due to the n^{th} current element may be broken into x and y components, where the x component value is denoted as $B_{1\text{xn}} = A_n e^{j(\omega t+\varphi_n)}\alpha_{nx}e^{jb_{nx}}$, where A_n and φ_n represent the n^{th} element's current magnitude and phase respectively, ω is the Larmor frequency, and the term $a_{nx}e^{jb_{nx}}$ describes the remainder of the steady-state geometrical phase shift and magnitude relation between the n^{th} drive and the x direction B_1 magnitude at a given point in the phantom. A similar equation was written for the y component of the B_1 field. The final x and y directional B_1 fields were then calculated as the

sum over n of B_{1xn}. The overall field was be found from these two quantities. Using the finite element simulations, the quantities $a_{nx}e^{jb_{nx}}$ and $a_{ny}e^{jby}$ were found for each point on a grid in the phantom placed on the selected FOV and for each current element on the coil. Using this information, field distributions were calculated from arbitrary current element magnitudes and phase angles. In the final step we determined each A_n and φ_n to obtain a distribution approximating a desired B_1 field distribution. To accomplish this, a cost function was defined for variations from the desired distribution, and then an iterative optimization algorithm was applied.

RF Coil Design—Transmission line (TEM) design approaches have demonstrated benefits for high-frequency RF coils (5,16,19,25). Importantly, independent TEM elements can be driven, received, and controlled for straightforward implementation with the parallel transceiver described above. Both linear and loop transmission line elements were evaluated for 400-MHz head coil construction (25). The linear element generates a flux vector that is typically parallel to the sample surface, and the loop generates a perpendicular vector. The linear element is shorter for a given coil length, and therefore is more efficient electrically at high frequencies. The coil comprised of linear elements also generates a more uniform field, especially in the periphery of its volume. The phase angles of the current on the linear array mimic those of other TEM or birdcage coils, and are incrementally phased over 360° to generate a theoretically uniform transverse field through the coil volume. In the loop array, however, currents in adjacent element legs are in approximate phase opposition, resulting in severe phase gradients in the RF field near the elements of the coil. Accordingly, a TEM coil with linear elements demonstrated the preferred properties for the 9.4T head coil design.

While RF nonuniformities can be actively controlled by methods described thus far, there are a number of considerations regarding the passive-coil design. For the multichannel TEM head-coil design, parameters include the length, i.d., o.d., and shape of the coil; the number, dimensions, and spacing of the TEM elements; the choice of dielectric material properties and dimensions; the relative degree of coupling or decoupling between the elements; and the positioning of the head within the coil. The coil model of Fig. 4 gives examples of these criteria. The eight-element coil model of Fig. 4a was designed to closely fit for strongest coupling to the head, and decoupling with neighboring elements. Also promoting the decoupling of neighboring elements is a thin layer of an efficient, nonprotonated, high dielectric constant substrate, such as Teflon. Teflon doubles the electrical distance between elements relative to air. Keeping the dielectric region thin further minimizes flux coupling between elements. The resulting coil is well suited for high-SNR, parallel imaging applications. However, RF uniformity suffers due to steep B_1 field magnitude and phase gradients, and interference patterns close to the coil elements. RF artifacts are seen as the sharp, asymmetrically positioned field null in the upper left-hand quadrant of Fig. 4b. Conversely, greater RF uniformity can be achieved by spacing the elements farther from the head and with a thicker dielectric region of lower dielectric constant, as shown in Fig. 4c. The resulting B_1 field will be more uniform and symmetric, as shown in Fig. 4d, though with greater mutual inductance between elements, and with less sensitive coupling to the head. Such trade-offs are correlated to the application requirements.

Based on these design methods and considerations, two initial multichannel TEM head coils were built. Both coils were close-fitting "brain coils" with an i.d. of 23 cm, an o.d. 25.5 cm, and length of 15.3 cm. One coil had eight elements and the other had 16 elements (Fig. 1d). The TEM elements of both consisted of an inner copper conductor 1.3 cm wide, an outer copper element 5 cm wide, and a Teflon dielectric layer 1.3 cm wide. Geometric spacing of the eight-element coil required no additional reactive decoupling. Approximately 1 pF was required to decouple neighboring elements of the 16-element coil by at least 18 dB. Decoupling capacitance bridging the elements was added with variable capacitors (NMAF 4HV; Voltronics Corp., Denville, NJ, USA) to allow for fine tuning of the head-loaded coil. Decoupling preamplifiers were not needed. Each coil element was tuned and matched to its respective transceiver channel by variable shunt and series capacitances (Voltronics NMNT 10-6). To better fit the Caucasian head shape of most of the volunteers, the eight-element coil was later reshaped into an ellipsoid with major and minor axes measuring 24.5 and 20.5 cm, respectively.

RF Safety—9.4T is above the 8T limit for the FDA Non-Significant Risk status. Before human images could be attempted, an Investigational Device Exemption (IDE) was required for human studies at this unprecedented field strength. The IDE was in turn required for local Internal Review Board (IRB) approval. One of the key requirements for these regulatory clearances was new safety data applicable to RF heating at 400 MHz. To obtain such data, an experiment was designed to identify the FDA-guideline limit for RF-induced temperature elevation vs. RF input power vs. time in a porcine model of the human head in vivo. For continuous wave power settings of 12–20 W, temperature vs. time was directly measured by fluoroptic thermometry, and recorded for human-adult-sized farm pigs (50–100 kg). In the experiment, anesthetized pigs were instrumented with fluoroptic probes inserted through burr holes over an array of model-guided positions in their scalp and brain. The pigs were then fitted with a head coil of the same design and dimensions to be used in human studies. RF power was then uniformly applied at continuous wave (CW) power level increments starting at 12 W. The pigs' heads weighed approximately 4 – 6 kg, which is similar to the weight of a human head and neck. Temperature vs. time was then recorded until the FDA guideline limit of 1°C above core temperature was reached (Figs. 5 and 6). In this way, an approximate correlation could be made between monitored RF power and FDA thermal limits for 400 MHz power input to a human-sized model with perfusion metabolic heating, and other healthy, normal thermoregulatory reflexes intact.

RESULTS AND DISCUSSION

Safety

In accordance with IDE and IRB requirements for conducting human studies at 9.4T, we investigated and monitored B_1 and B_0 bio-effects and subject safety. For a given RF excitation sequence, increased energy is lost to the tissue conductor and dielectric due to the very short Larmor wavelength in high water content and high conductivity tissues at 400 MHz, compared to lower field strengths. A consequence of this energy loss is RF heating, a potential safety concern. While significant safety concerns were not interpreted from subchronic exposure of rats to 9.4T (30), the first use of 9.4T for human studies compels

close observation of subjects who are exposed to such a high field. The preliminary results from initial animal models and human studies are given below.

RF Heating—The FDA maximum temperature guideline limit of 1°C above core temperature is first reached well into the brain; however, calculations have shown that SAR and ΔT are greatest in the more peripheral brain and scalp (11,31,32) (Fig. 6). Depending on the animal, 2.4 – 4.0 W/kg RF power input to a head coil would require 3 hr or more to raise the temperature of the perfused pig brain to the guideline limit. Most MRI studies can be conducted well under this time limit. Therefore, time and temperature data taken together may be more useful. For example, 20 W RF power applied to the coil and a 5-kg head elevated the temperature in the brain by only 0.2°C during a 30-min time period, which is more typical of an NMR scan.

The fact that maximum absolute temperatures are first measured in the brain is not inconsistent with lower SAR and ΔT values in the brain compared to the scalp. Although the maximum temperature change may occur in the scalp, the scalp is well perfused and adjacent to an infinite, 22°C ambient heat sink. The healthy, normal thermal profile of a head (human or porcine) peaks in the brain of a subject that is maintained at core body temperature. When energy is added from a large head coil at a low rate, such as in an NMR study, the subject's core temperature and thermal profile across the head are raised as if the subject had a fever. In a well-perfused subject, the absolute temperature first reaches the FDA thermal limit in the brain.

9.4T Experience—All of the human subjects for the 9.4T studies were screened to be healthy normal volunteers. The MRI study was explained to each subject. The volunteer was told the objective of the study, the potential benefit to science (though not to the individual), and the potential risks of the study. As data accumulated from subject experience at 9.4T, they were shared with new volunteers during the preparation period; however, this may have influenced the exit-interview results. Any questions from the subjects were answered. The subjects were then asked to lie supine on a comfortably padded patient table, covered with a light blanket, and given earphones for communication and music of their choice, and a squeeze ball for communication. The close-fitting RF head coil (shown in Fig. 1d and modeled in Fig. 4a) was then placed over the volunteer's head. Each of the eight elements was tuned and matched, and connected to eight respective channels of the parallel transceiver (Fig. 1c). The volunteers were reminded that they could end the study for any reason at any time, and were then slowly rolled into position in the bore of the 9.4T magnet. The asymmetric head gradients give ample room in the bore space for the body and shoulders. The studies varied in duration from 1 to 2 hr. For the first 44 volunteers, no studies were prematurely terminated. All subjects were given exit interviews regarding their experience in the 9.4T exam. The notable comments from these interviews are reported in Table 1. The most common response—a feeling of "sleepiness"—may have resulted from the subjects spending an hour or two reclining in a dark, comfortable environment with calming music. Vertigo, dizziness, and light-headedness are common and fairly well understood acute side-effects of head movement at high fields. A "metallic taste" is also a familiar (though apparently harmless) complaint from experience at other field strengths as

well. The head gradients in these first studies were not driven at high dB/dt levels, so no mention was made of muscle twitching or loud noise levels.

B_1 Shimming

Early results for the programmable B_1 phase and magnitude control are shown in Fig. 7. To demonstrate this programmable B_1 field magnitude control capability, a 9.4T fast low-angle shot (FLASH) image data set was acquired with TR/TE = 50/5 ms, matrix = 256 × 128, FOV = 22 cm × 19 cm, and slice thickness = 5 mm. Each image in the Fig. 7a series shows a different gain setting, starting with the amplifiers disabled (far left), and then with equal gains added incrementally to each element in a clockwise pattern until all channels are driven (far right). The element phase angles traverse 360° in equal increments to circularly polarize the coil. The images are constructed by simple sum-of-squares magnitude addition without intensity correction. Phase control is demonstrated in Fig. 7b. Driving all elements with isomagnitude RF signal, the phase angles of all eight coil elements were set to isophase "0°" at the far left. Progressing to the right in Fig 7b, incrementally increasing 45° phase angles were added to each element around the coil in a clockwise direction until the coil was circularly polarized at the far right. The homogeneity (or other criteria) for these images can be further refined by algorithm and feedback-driven optimization routines (24).

The low-resolution FLASH images shown in Fig. 8 were acquired to qualitatively evaluate the RF excitation homogeneity during operator-prescribed B_1 shimming. The parameters for these images were TR/TE = 100 ms/4 ms, matrix = 256 × 128, and a 5-mm-thick 6° excitation pulse. Five slices were acquired (only the slice near the region that was being targeted for B_1 shimming is shown). Figure 8a is the default starting point, where the transmit magnitude for each coil is equal and the phase is circularly polarized in the elliptical TEM coil. The first scout image acquired in this initial coil configuration shows destructive interference that reduces the net B_1 on the left side of the brain. A new set of phases for the coil elements in this area was approximated by the operator and entered into the phase and gain controller, and a new image was acquired and processed. These steps took roughly 1 min per iteration when done manually. Four iterations later, the image in Fig. 8b shows improved RF homogeneity in the region of the initial artifact. Initial and correction coil element excitation phases are given in Fig. 8. The magnitude remained equal for each coil.

FLASH images with TR/TE = 150 ms/7 ms and a ~5° excitation acquired using this B_1 shim setting are shown in Fig. 9. The transverse image (Fig. 9a) corresponds to the target region for B_1 shimming. This image has a 512 × 400 acquisition matrix size for 0.5 mm × 0.5 mm × 2.0 mm resolution. Two averages were collected in 2 min. Additionally, coronal (Fig. 9b) and sagittal (Fig. 9c) images were acquired with the same B_1 shim setting. The parameters for these images were FOV = 25 × 20 cm, slice thickness = 5 mm, matrix size = 512 × 256, and four averages. The images are not intensity-corrected. Moderate shading is still visible across the image, but the signal voids seen in the starting scout image have been eliminated.

RF Localization—RF field uniformity and image homogeneity are not the only criteria for image optimization. By controlling these B_1 field gradients, one can optimize images of

selected ROIs for higher SNRs, lower power deposition (SAR), contrast, and other criteria. These ROIs may correspond to targeted organs or tissues. Localization and parametric optimization of these ROIs will be automated by feedback-driven algorithms, such as the simulated annealing method introduced in the preceding section. The simulated results of this approach are given in Fig. 10. In this example, the B_1 field magnitude is automatically maximized at an arbitrarily chosen location in a cylindrical phantom.

Intrinsic Contrast—Using the parallel transceiver and RF coils shown in Figs. 1 and 2, we used high-frequency field optimization methods employing console-driven, multichannel RF field magnitude and phase shimming to produce surprisingly homogeneous head images at 9.4T. The strong static field increases the susceptibility contrast. With the use of a long TE to enhance T_2* contrast, and slightly thicker slices, additional structures are revealed. Figure 11 shows an intensity-corrected 9.4T FLASH image that contrasts the medulary veins, Virchow-Robins spaces, possible tracts, and other features. The acquisition parameters were TR/ TE = 50/9 ms, 7° excitation, NEX = 8, matrix = 512 × 512, 22 cm × 19 cm, and slice thickness = 6 mm.

The history of NMR is rich with fortuitous paradoxes in that anticipated high-field problems, such as the deoxygenated blood susceptibility artifact, have been harnessed as new tools. RF artifacts due to extremely short brain and muscle tissue wavelengths of 12 cm at 7T and 9 cm at 9.4T will become the increasingly powerful RF shims and gradients used to localize ROIs and to optimize selected criteria therein by new families of RF protocols and feedback-driven optimization algorithms. Shorter wavelengths bring a new ability to "steer" RF fields to targeted anatomies and acquisition mechanisms. The problem that every element of a TEM coil must be independently tuned (in contrast to monolithic birdcage resonators) becomes a solution for B_1 field control because every element can be tuned to manipulate the B_1 field component of each with high sensitivity. Implementation of phase and magnitude control is well served by a multichannel TEM coil interfaced to the parallel transceiver reported.

CONCLUSIONS

Preliminary results from initial 9.4T studies indicate that safe and successful human head imaging is feasible at this field strength. To achieve these results, significant new technologies and methodologies were advanced. A 9.4T superconducting magnet of human bore size was developed. A parallel transceiver front end was invented to provide console control for new methods of RF shimming and parallel imaging. This new transceiver is now being employed to develop new feedback-driven, interactive, and automated ROI targeting and image optimization algorithms. 9.4T Larmor wavelengths that are significantly shorter than anatomic dimensions are making these new concepts in image localization and optimization possible.

Acknowledgments

Grant sponsor: National Institutes of Health; Grant numbers: NIH-S10 RR139850; NIH-R01 EB000895-04; NIH-P41 RR08079; Grant sponsor: Keck Foundation.

References

1. Vaughan, J.; Garwood, M.; Merkle, H.; Adriany, G.; Uckun, F.; Ugurbil, K. First 9.4T homogeneous head imaging of a monkey. Proceedings of the 82nd Annual Meeting of RSNA; Chicago, IL, USA. 1996. p. 292
2. Barfuss H, Fischer H, Hentschel D, Ladebeck R, Oppelt A, Wittig R, Duerr W, Oppelt R. In vivo magnetic resonance imaging and spectroscopy of humans with a 4 T whole-body magnet. NMR Biomed. 1990; 3:31–45. [PubMed: 2390452]
3. Bomsdorf H, Helzel T, Kunz D, Roschmann P, Tschendel O, Wieland J. Spectroscopy and imaging with a 4 tesla whole-body MR system. NMR Biomed. 1988; 1:151–158. [PubMed: 3275125]
4. Ugurbil K, Garwood M, Ellermann J, Hendrick K, Hinke R, Hu X, Kim S-G, Menon R, Merkle H, Ogawa S, Salmi R. Imaging at high magnetic fields: initial experiences at 4T. Magn Reson Q. 1993; 9:259–277. [PubMed: 8274375]
5. Vaughan J, Hetherington H, Otu J, Pan J, Pohost G. High frequency volume coils for clinical nuclear magnetic resonance imaging and spectroscopy. Magn Reson Med. 1994; 32:206–218. [PubMed: 7968443]
6. Vaughan, J.; Gonzalez, R. A 9.4T NMR imaging system for primate research. 1997. NIH-SIO RR139850
7. Vaughan J, Garwood M, Collins C, DelaBarre L, Adriany G, Andersen P, Merkle H, Smith M, Ugurbil K. 7T vs. 4T: RF power, homogeneity and signal-to-noise comparison in head images. Magn Reson Med. 2001; 46:24–30. [PubMed: 11443707]
8. Beck B, Plant D, Grant S, Thelwall P, Silver X, Mareci T, Benveniste H, Smith M, Collins C, Crozier S. Progress in MRI at the University of Florida. MAGMA. 2002; 47:579–593.
9. Zhang, N.; Roos, M.; Vaughan, J.; Budinger, T. Head coil B_1 field inhomogeneity and SNR performance at 8–10T. Proceedings of the 4th Annual Meeting of ISMRM; New York, NY, USA. 1996. p. 252
10. Harrison, J.; Vaughan, J. Finite element modeling of head coils for high frequency magnetic resonance application. 12th Annual review of progress in applied computational electromagnetics; Monterey, CA: Naval Postgraduate School; 1996.
11. Collins C, Li S, Smith M. SAR and B_1 field distributions in a heterogeneous human head model within a bird cage coil. Magn Reson Med. 1998; 40:847–856. [PubMed: 9840829]
12. Ibrahim T, Lee R, Abduljalil A, Baertlein B, Robitaille PML. Dielectric resonances and B_1 field inhomogeneity in UHFMRI: computational analysis and experimental findings. Magn Reson Imaging. 2001; 19:219–226. [PubMed: 11358660]
13. Ibrahim TS, Lee R, Baertlein BA, Abduljalil AM, Zhu H, Robitaille PML. Effect of RF coil excitation on field inhomogeneity at ultra-high fields: a field optimized TEM resonator. Magn Reson Imaging. 2001; 19:1339–1347. [PubMed: 11804762]
14. Yang QX, Wang JH, Zhang XL, Collins CM, Smith MB, Liu HY, Zhu XH, Vaughan JT, Ugurbil K, Chen W. Analysis of wave behavior in lossy dielectric samples at high field. Magn Reson Med. 2002; 47:982–989. [PubMed: 11979578]
15. Keltner J, Carlson J, Roos M, Wong S, Wong T, Budinger TF. Electromagnetic fields of surface coil in vivo NMR at high frequencies. Magn Reson Med. 1991; 22:467–480. [PubMed: 1812380]
16. Vaughan J, Adriany G, Snyder C, Tian J, Thiel T, Bolinger L, Liu H, DelaBarre L, Ugurbil K. Efficient high-frequency body coil for high-field MRI. Magn Reson Med. 2004; 52:851–859. [PubMed: 15389967]
17. Van de Mortele P-F, Akgun C, Adriany G, Moeller S, Ritter J, Collins C, Smith M, Vaughan J, Ugurbil K. B_1 destructive interferences and spatial phase patterns at 7 tesla with a head transceiver array coil. Magn Reson Med. 2005; 54:1503–1518. [PubMed: 16270333]
18. Tannus, A.; Garwood, M. Reducing RF power requirements of multislice imaging using a single adiabatic frequency swept inversion pulse. Proceedings of the 4th Annual Meeting of ISMRM; New York, NY, USA. 1996. p. 362
19. Vaughan, J. Massachusetts General Hospital, assignee. RF coil for imaging system. U.S. patent 6,633,161. 2003.

20. Collins C, Liu W, Swift B, Smith M. Combination of optimized transmit arrays and some receive array reconstruction methods can yield homogeneous images at very high frequencies. Magn Reson Med. 2005; 54:1327–1332. [PubMed: 16270331]
21. Hoult D. Sensitivity and power deposition in a high-field imaging experiment. J Magn Reson Med. 2000; 12:46–67.
22. Stenger, V.; Saekho, S.; Zhengui, Z.; Yu, S.; Boada, F. B1 Inhomogeneity reduction with transmit SENSE. Proceedings of the 2nd International Workshop on Parallel MRI; Zurich, Switzerland. 2004. p. 94
23. Collins, C.; Beck, B.; Fitzsimmons, J.; Blackband, S.; Smith, M. Strengths and limitations of pulsing coils in an array sequentially to avoid RF interference in high field MRI. Proceedings of the 13th Annual Meeting of ISMRM; Miami Beach, FL, USA. 2005. p. 816
24. Vaughan, J.; Adriany, G.; Ugurbil, K.; Strupp, J.; Andersen, P. University of Minnesota, assignee. Parallel transceiver for nuclear magnetic resonance system. U.S. patent 6,969,992. 2005.
25. Adriany G, Van de Mortele P-F, Wiesinger F, Moeller S, Strupp J, Andersen P, Snyder C, Zhang X, Chen W, Pruessmann K, Boesiger P, Vaughan J, Ugurbil K. Transmit and receive transmission line arrays for 7 tesla parallel imaging. Magn Reson Med. 2005; 53:434–445. [PubMed: 15678527]
26. Vaughan T, DelaBarre L, Snyder C, Tian J, Bolan P, Garwood M, Adriany G, Strupp J, Andersen P, Van de Moortele P-F, Ugurbil K. Highest field human MR imaging. IEEE Trans EMC. 2006:213.
27. Vaughan, J. University of Alabama, Birmingham, assignee. High frequency volume coils for nuclear magnetic resonance applications. U.S. patent 5,557,247. 1996.
28. Vaughan, J.; Adriany, G.; Ugurbil, K. University of Minnesota, assignee. Shim, gradient, and parallel imaging coil. U.S. patent 10/420,541. 2003.
29. Vaughan, J.; DelaBarre, L.; Snyder, C.; Adriany, G.; Collins, C.; Van de Moortele, P-F.; Moeller, S.; Ritter, J.; Strupp, J.; Andersen, P.; Tian, J.; Smith, M.; Ugurbil, K. RF image optimization at 7T and 9.4T. Proceedings of the 13th Annual Meeting of ISMRM; Miami Beach, FL, USA. 2005. p. 953
30. High W, Sikora J, Ugurbil K, Garwood M. Subchronic in vivo effects of a high static magnetic field (9.4T) in rats. J Magn Reson Imaging. 2000; 12:122–139. [PubMed: 10931572]
31. McDuffie, J.; Harrison, J.; Pohost, G.; Vaughan, J. 3D numerical modeling of high frequency volume coils for clinical NMR. Proceedings of the 3rd Annual Meeting of SMR; Nice, France. 1995. p. 185
32. Sorensen, A.; Wu, O.; Yamada, K.; Vaughan, J. MRI at 3.0 tesla: preliminary ex-vivo animal and in-vivo human safety studies. Proceedings of the 9th Annual Meeting of ISMRM; Glasgow, Scotland. 2001. p. 1762

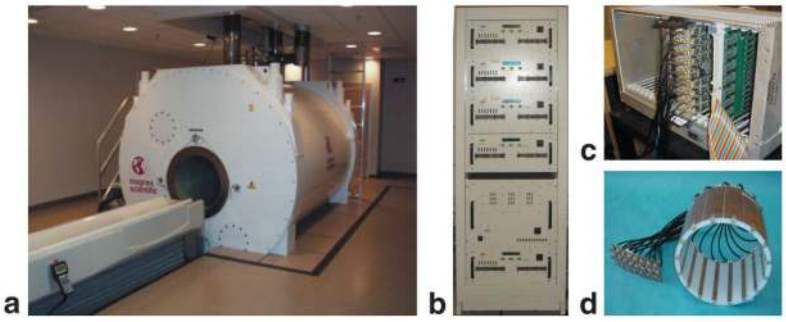

FIG. 1.

Hardware developed for 9.4T imaging. **a:** The Magnex Scientific 65-cm bore magnet. **b:** A rack of 5, 500-W broadband RF power amplifiers (top) together with an 8-bit digital phase and gain controller (near bottom). Two more racks hold the additional 11 power amplifiers to complete the 16-channel parallel transmitter reported here. **c:** ADC boards for the 16-channel parallel receiver. **d:** A capacitively decoupled 16-channel, 400-MHz stripline TEM resonator.

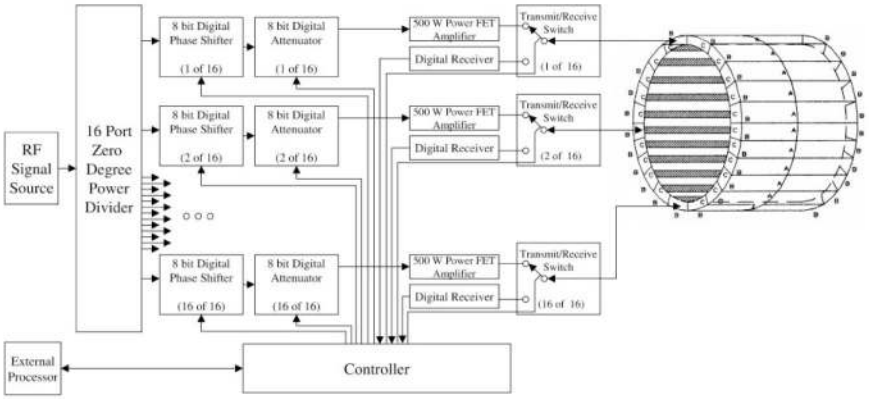

FIG. 2.

Schematic of a parallel transceiver. Phase and gain are controlled with 8-bit resolution on multiple independent transmit channels. Transmit and receive functions are separated in time by a transmit-receive switch on each channel. Each receive channel incorporates a decoupling preamp, filters, and receiver gain as needed. Each transmit channel includes a 500-W solid-state power amplifier with feedback for the RF power monitor. The RF power amplifiers are broadbanded to facilitate the addition of a programmable frequency synthesizer for multinuclear control.

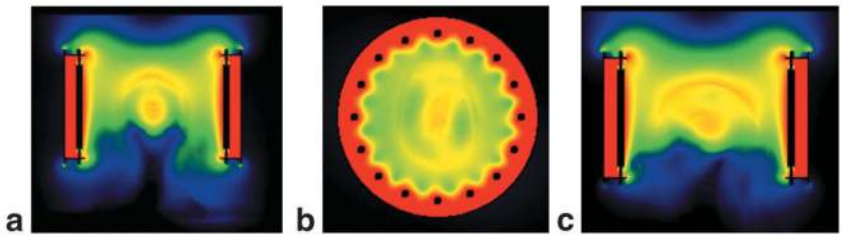

FIG. 3.

9.4T predictions of B_1 nonuniformities in a head with a homogeneous circularly polarized coil. Each color change represents a 20-dB field gradient.

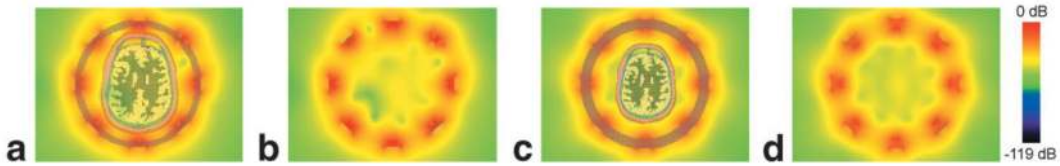

FIG. 4.

Multichannel TEM head-coil design considerations. **a:** FDTD calculations of B_1 for a head inside a close-fitting, eight-channel TEM coil with a thin dielectric substrate (blue shaded ring) at 400 MHz. **b:** The head template overlay is removed to better show the RF artifacts. **c** and **d:** B_1 calculations for the head inside a roomier coil with a thicker dielectric substrate.

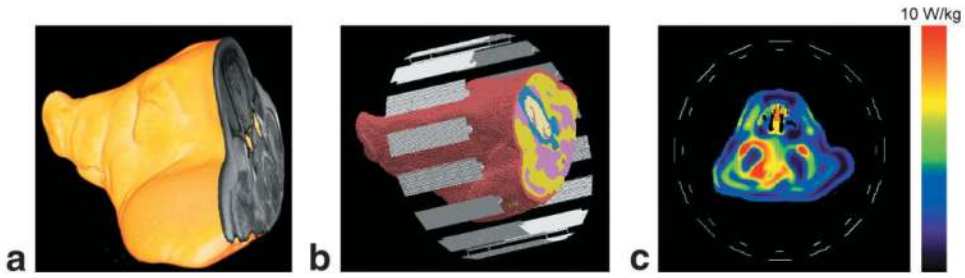

FIG. 5.

Modeling SAR in a porcine head. **a:** Imaged porcine head. **b:** The anatomy from this 3D image was segmented, assigned frequency-and tissue-specific permittivity and conductivity values, and assembled into a model within a 16-element TEM volume coil. **c:** SAR contours calculated by the XFTTD method. Such models guide fluoroptic probe placement for experimental studies and further understanding of SAR and heating induced by high-frequency fields.

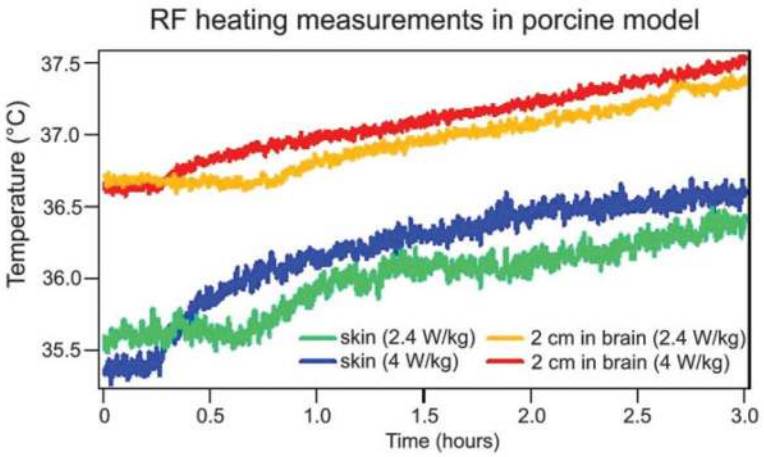

FIG. 6.

RF heating at 9.4T. The temperature vs. time vs. applied continuous-wave RF power is measured by implanted fiber-optic probes. The plot is the average heating recorded from 12 human-sized anesthetized porcine heads in a head coil tuned to 400 MHz.

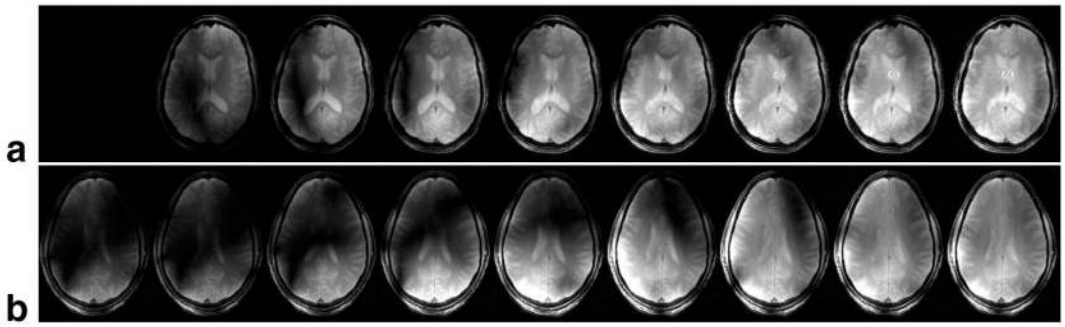

FIG. 7.

B_1 shimming with the parallel transceiver and an eight-channel TEM coil at 9.4T. **a:** A series of B_1 field shimming steps, left to right, adjusting the field magnitude only. **b:** B_1 shimming performed by adjusting only the phase angle of the transmit signal. In practice, both B_1 magnitude and phase will be adjusted together to optimize image criteria by automated feedback-driven algorithms.

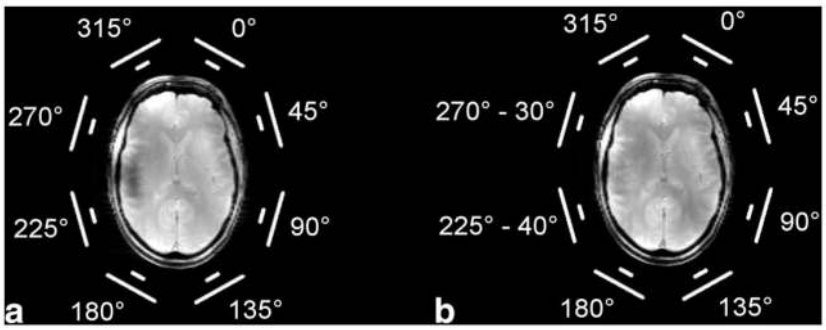

FIG. 8.

Effect of the transmit phase on image homogeneity. **a:** Scout FLASH image of a head inside a circularly polarized elliptical coil. The loss of signal near the left ear is the result of destructive interference reducing the net B_1^+. The relative transmit phase for each coil labeled near the two lines representing the conductor and ground planes of each coil is shown. **b:** By adjusting only the relative transmit phase of the coils, local destructive interference can be reduced.

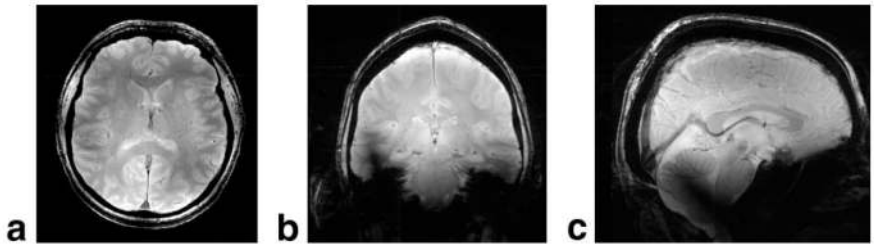

FIG. 9.

B_1-shimmed FLASH images. Using the relative transmit phases shown in Fig. 8b, transverse (**a**), coronal (**b**), and sagittal (**c**) images of the same subject were acquired.

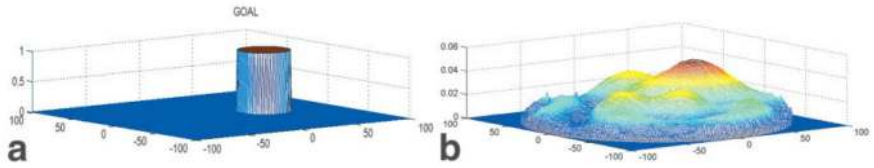

FIG. 10.

RF model of B_1 localization in a cylindrical phantom. **a:** An off-center target B_1 distribution was defined in the center slice of a finite-element model of a head-sized cylindrical phantom placed in a 16-rung TEM coil. **b:** B_1 magnitude optimization was achieved by iteratively varying both the phase and magnitude of each of 16 line currents in a simulated annealing approach.

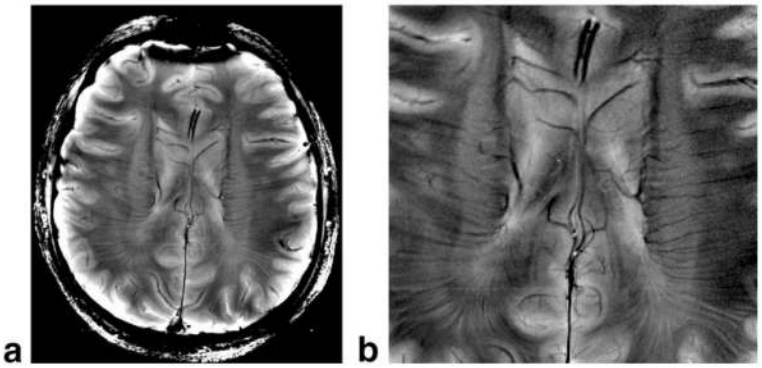

FIG. 11.

Initial 9.4T FLASH images showing T_2* contrasted venous structure and other features. **a:** The dark band at the top is an uncorrected B_0 artifact.

Table 1

Comments From the First 44 Healthy Normal Human Volunteers Studied at 9.4T

Sleepiness	24
Metallic taste	14
Vertigo/dizziness	11
Lightheadedness	8
Cold	7
Warmth	2
Nausea	2